Unsupervised stratification of patients with myocardial infarction based on imaging and in-silico biomarkers

Dolors Serra, Pau Romero, Paula Franco, Ignacio Bernat Miguel Lozano, Ignacio Garcia-Fernandez, David Soto, Antonio Berruezo, Oscar Camara and Rafael Sebastian,

***Abstract*— This study presents a novel methodology for stratifying post-myocardial infarction patients at risk of ventricular arrhythmias using patient-specific 3D cardiac models derived from late gadolinium enhancement cardiovascular magnetic resonance (LGE-CMR) images. The method integrates imaging and computational simulation with the fast electrophysiology solver, Arritmic3D, enabling rapid and accurate ventricular arrhythmias (VA) risk assessment in clinical timeframes. Applied to 51 patients, the solver generated thousands of personalized simulations exploring ranges of values for several parameters to evaluate arrhythmia inducibility and predict VA risk. Key findings include the identification of slow conduction channels (SCCs) within scar tissue as critical to reentrant arrhythmias and the localization of high-risk zones for potential intervention. The Arrhythmic Risk Score (ARRISK), developed from simulation results, demonstrated strong concordance with clinical outcomes and outperformed traditional imaging-based risk stratification. The methodology is fully automated, requiring minimal user intervention, and offers a promising tool for improving precision medicine in cardiac care by enhancing patient-specific arrhythmia risk assessment and guiding treatment strategies.**

***Index Terms*— Ventricular Arrhythmia Risk, Fast Eikonal Solver, LGE-CMR Imaging, Patient-specific therapy, Cardiology Computational Simulation**

I. Introduction

PREDICTING ventricular arrhythmias in post-myocardial infarction patients, especially in the early phase, remains a significant clinical challenge due to the elevated risk of sudden death. Early implantable cardioverter-defibrillator placement does not significantly improve mortality [1]. Postinfarct ventricular tachycardia typically arises as a reentrant arrhythmia sustained by circuits formed by surviving myocardial strands in scar tissue, where slow conduction channels (SCC) exhibit reduced gap junction density and impaired excitability [2]. LGE-CMR can identify SCCs to guide catheter ablation, though it remains challenging due to the difficulty in locating optimal targets and the potential for extensive lesions [3], [4].

Precision medicine in clinical prognosis aims to provide personalized therapies for each patient. The concept of a digital twin enables the integration of patient-specific clinical data [5]. In cardiology, combining patient-specific simulations with clinical metrics can improve the prediction of ventricular arrhythmia risks and enhance the identification of problematic areas [6].

Advanced biophysical models simulate cellular electrical dynamics, pathological changes, and drug responses [7], [8]. These models are used for simulating ventricular tachycardia (VTs) due to their ability to model ischemic tissue's heterogeneous properties [9]–[13]. However, they require high spatial and temporal discretization, leading to lengthy computation times. Despite advances in multi-GPU computations, the complexity and hardware demands limit clinical application. Simplified computational models have emerged to address this issue, offering accurate results suitable for clinical use [14]–[16].

To integrate imaging with computer simulation technology in clinical practice, we propose a methodology for estimating ventricular arrhythmia risk using image-based personalized 3D models that can be executed in clinical timeframes. This approach utilizes Arritmic3D, a physiological cellular automaton derived from thousands of pre-computed biophysical simulations, coupled with an Eikonal model [17]. It accurately reproduces cellular and tissue heterogeneity with low spatial and temporal discretization, allowing for rapid computation on desktop computers.

This study demonstrates the potential of simplified electrophysiological simulations for arrhythmia risk assessment, applied to a cohort of 51 myocardial infarction patients. The use of Arritmic3D enabled thousands of patient-specific simulations, covering various risk scenarios and individual variabilities. The method is fully automated post-segmentation, requiring no manual intervention, and completes in minutes,

 Corresponding author: Miguel Lozano. This research was funded by Generalitat Valenciana Grant AICO/2021/318 (Consolidables 2021) and Grant PID2020-114291RB-I00 funded by MCIN/ 10.13039/501100011033 and, by "ERDF A way of making Europe"; D.S. was funded by the Generalitat Valenciana and the European Social Fund (FSE) through the Recruitment of Predoctoral Research Staff ACIF/2021/394 included in the FSE Operational Program 2021-2025 of the Valencian Community (Spain);.

D. Serra, P. Romero, M. Lozano, I. Garcia-Fernandez and R. Sebastian are with CoMMLab, Departament d'Informatica, Universitat de Valencia, Spain (email: miguel.lozano@uv.es)

P. Franco, I. Bernat and O. Camara are with Universitat Pompeu Fabra, Barcelona, Spain

D. Soto and A. Berruezo Cardiology Department, Heart Institute, Teknon Medical Center, Barcelona, Spain

highlighting its efficiency and clinical applicability. The research details the methodology, presents simulation results, and compares the predicted arrhythmia risk with clinical follow-up data.

II. Material and Methods

A. Patient dataset

Patients with chronic myocardial infarction were recruited at the Teknon Clinical Center (Barcelona, Spain), where they underwent late gadolinium enhancement cardiovascular magnetic resonance (LGE-CMR) scans for detailed heart imaging. The images were acquired using a 1.5-Tesla scanner (MAGNETOM TrioTM, Siemens Healthcare, Erlangen, Germany) with a resolution of 1 mm between planes and an isotropic in-plane resolution of 0.9 mm, producing 120 slices per scan. The LGE-CMR scans utilized the 3D-DIXON imaging technique. This high resolution is crucial for accurately reconstructing pathological tissue in patient-specific computational cardiac models [18].

For each patient, the clinical data includes whether the patient experienced VT, whether VT inducibility was attempted in the clinic, and if so, whether the attempt was successful. Additionally, a risk classification is provided. VT episodes are categorized as HIGH risk when identified as sustained monomorphic VT (SMVT, characterized by regular QRS morphology) or Polymorphic VT (with varying QRS complex morphology) due to their potential severity. They are classified as LOW risk when identified as non-sustained VT (NSVT), and as ZERO risk when VT was neither experienced nor induced. Data for the complete cohort of 51 patients are available in Table I. Note that the naming of the cases is arbitrary and does not have any particular meaning, corresponding to the internal labels used by clinicians for this cohort. In particular, the last three patients, labelled as P5_P, P11_P and P12_P have no relation with patients P5, P11 and P12.

B. Digital Twin Construction

The anatomical model for each patient was constructed through the segmentation of LGE-CMR image scans. The ADAS3D software (Galgo Medical, Barcelona) was used to segment the endocardial and epicardial surfaces, defining the closed heart boundaries. The scar region was segmented using the maximum intensity pixel method, as implemented in ADAS3D, with a default 40-60 pixel-signal-intensity (PSI) threshold under expert supervision. This process allowed for differentiation between the border zone (BZ), scar core zone (CZ), and healthy tissue within the scar region. The entire segmentation process took approximately 10 minutes per patient. From these LGE-CMR scans, volumetric models were generated, and clinical biomarkers were calculated (summarized data available in Fig. 1). Additionally, the SCC centerlines are obtained via the Adas3D segmentation algorithm, only for visualization purposes in our figures (e.g., Figs. 2 and 5. The Arritmic3D solver internally uses the native segmentation of BZ, Core, and healthy tissue without precomputed SCCs. This ensures that simulations remain independent of external SCC segmentations.

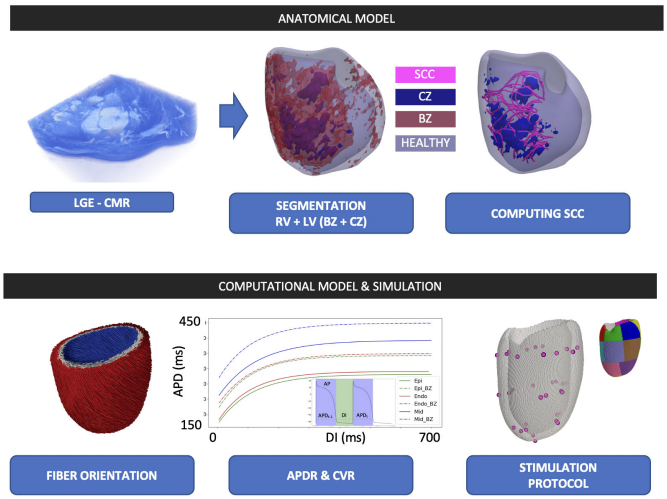

Fig. 1. LGE-CMR-based Digital Twin construction workflow and data preprocessing for simulations.

Using the segmented surfaces, we constructed a digital twin for each patient. The voxelization of the models was directly derived from the LGE-CMR stacks, which provided an isotropic resolution of approximately 1 mm. Subsequently, the nodes and elements of the models were labeled according to the cellular populations located in the endocardial, mid-myocardial, and epicardial regions, based on their position across the myocardial wall [19]. Labels for healthy, BZ, or CZ tissue were applied to adjust the conduction velocity restitution (CVR) and action potential duration restitution (APDR) curves accordingly.

All clinical cases exhibited complex scar and SCC structures (represented by magenta tubes in Fig. 2), regardless of whether the patients had experienced clinical arrhythmic events. Fiber orientation was determined using a rule-based model, specifically the Streeter model [20], and was incorporated as a property of the model's elements. It is important to note that the entire post-segmentation process for creating the digital twins was fully automated, requiring no manual user intervention and taking approximately 2 minutes per case.

C. Fast Electrophysiology Solver

Once the digital twins are built, we simulated heart activation using Arritmic3D, a fast, event-based electrophysiology solver [17]. Arritmic3D was selected for the experiments due to its computational efficiency, achieving simulation times 100x faster than openCARP, without compromising accuracy for risk stratification. This efficiency allows for large-scale clinical simulations that explore ranges of parameter values, which would otherwise be impractical with high-fidelity biophysical solvers.

The tissue is discretized in a grid of nodes that represent small portions of cardiac tissue. The simulation follows a discrete event-driven approach, where nodes transition between two states: inactive (repolarized) and active (depolarized). Activation occurs through neighboring nodes via a wavefront propagation mechanism, determined by local conduction ve-

PAT.	LV MASS (g)	BZ (g)	CZ (g)	SCC(g)	LVEF (%)	AGE	SEX	VT	Sim Time (h)	Effective sims	#VT	#VT base-line	ARRISK	Clinical risk
P1	82.18	4.45	0.64	0	66	71	M	N-X-N	15	1998	0	0	ZERO	ZERO
P2	109.10	13.36	3.48	8.05	36	53	M	P-P-P	20	1934	22	16	HIGH	HIGH
P3	100.88	4.65	0.51	0	61	63	M	N-X-N	22	1884	0	0	ZERO	ZERO
P4	67.81	3.50	2.48	2.37	63	74	F	N-X-P	10	1506	1	1	LOW	ZERO
P5	197.65	42.21	5.36	21.09	28	84	M	N-P-P	27	1830	23	10	HIGH	HIGH
P6	73.46	2.74	0.56	0.55	69	48	F	N-X-N	12	1812	0	0	ZERO	ZERO
P7	79.80	25.74	3.96	14.94	47	78	F	N-X-P	12	1656	10	9	LOW	ZERO
P8	90.65	1.98	0.56	0	58	56	M	N-X-N	14	1787	0	0	ZERO	ZERO
P9	111.51	10.35	3.91	1.94	63	78	M	N-X-P	19	1966	5	3	LOW	ZERO
P10	120.34	5.56	1.50	0.85	63	68	M	N-X-P	22	1764	1	1	LOW	ZERO
P11	109.81	9.22	2.48	0.64	30	54	M	N-X-N	15	1818	0	0	ZERO	ZERO
P12	115.85	24.25	12.58	9.06	47	70	M	P-X-P	18	1830	7	3	LOW	LOW
P13	81.80	2.48	0.75	1.28	63	58	M	N-X-N	13	1644	0	0	ZERO	ZERO
P14	179.37	53.20	35.41	35.19	40	39	M	N-X-P	20	1782	27	14	HIGH	ZERO
P15	100.79	8.44	1.15	0	59	69	M	N-X-N	19	1860	0	0	ZERO	ZERO
P16	195.69	27.72	12.72	2.33	41	66	M	N-X-P	26	1938	13	10	LOW	ZERO
P18	146.47	7.11	4.65	2.35	46	63	M	P-X-P	26	1926	2	1	LOW	LOW
P19	89.10	6.59	4.53	0.63	48	49	M	N-X-N	13	1884	0	0	ZERO	ZERO
P20	151.43	3.92	1.87	0	44	41	M	N-X-N	24	1998	0	0	ZERO	ZERO
P21	96.76	8.04	2.03	2.02	60	56	M	N-X-P	17	1990	2	2	LOW	ZERO
P23	105.94	13.76	4.82	3.59	57	63	M	P-N-P	20	2020	3	3	LOW	LOW
P24	110.26	14.78	3.91	10.21	47	64	M	N-X-P	13	1788	1	1	LOW	ZERO
P26	137.54	13.22	6.21	2.81	57	61	M	N-X-P	35	2022	26	16	HIGH	ZERO
P28	60.24	1.12	0.13	0	56	47	F	N-X-P	19	1860	5	0	LOW	ZERO
P29	108.39	20.34	3.67	14.35	55	80	F	N-X-P	19	1914	2	2	LOW	ZERO
P30	139.80	8.10	9.02	0.24	43	75	F	N-X-N	17	1956	0	0	ZERO	ZERO
P32	123.38	18.55	4.11	7.97	49	73	F	N-X-P	18	1842	4	2	LOW	ZERO
P33	105.41	17.02	1.59	5.72	57	49	F	N-X-P	17	1962	1	1	LOW	ZERO
P34	87.28	11.80	1.75	1.28	60	70	M	N-X-N	11	1560	0	0	ZERO	ZERO
P35	115.95	18.06	5.99	8.39	65	73	M	N-X-P	14	1956	1	1	LOW	ZERO
P36	101.41	22.24	4.74	15.14	32	61	M	N-X-P	15	2010	6	3	LOW	ZERO
P37	206.77	65.73	40.76	22.97	35	49	M	N-P-P	20	2058	25	16	HIGH	HIGH
P38	151.15	18.15	4.09	1.68	34	68	M	N-N-P	19	2094	19	11	HIGH	ZERO
P39	107.16	3.84	0.54	0	66	69	M	N-X-N	16	2052	0	0	ZERO	ZERO
P41	108.81	19.93	5.93	8.54	62	62	M	N-X-P	16	1908	29	16	HIGH	ZERO
P43	102.27	5.66	1.07	1.54	60	49	M	N-X-N	19	2014	0	0	ZERO	ZERO
P44	157.07	34.19	22.94	15.39	32	61	M	N-P-P	24	2055	36	19	HIGH	HIGH
P45	181.73	52.19	13.30	28.55	38	74	M	N-P-P	24	1968	31	15	HIGH	HIGH
P46	149.56	15.37	2.13	3.24	39	69	M	P-P-P	30	1962	26	11	HIGH	HIGH
P48	105.46	19.93	2.1	8.91	39	72	M	N-N-N	19	1918	0	0	ZERO	ZERO
P49	87.27	7.8	0.98	0.8	49	57	M	N-X-N	15	1698	0	0	ZERO	ZERO
P52	97.13	13.09	4.81	5.61	35	70	M	N-P-P	16	1972	1	0	LOW	HIGH
P53	135.17	40.98	29.08	23.37	30	66	M	N-P-P	13	1962	21	11	HIGH	HIGH
P54	108.17	4.52	3.43	2.08	51	27	M	N-X-N	20	1770	0	0	ZERO	ZERO
P55	118.09	7.46	9.57	2.34	42	68	M	N-X-N	19	2088	0	0	ZERO	ZERO
P56	99.52	3.45	1.32	0	55	50	M	P-X-N	19	1984	0	0	ZERO	LOW
P57	79.95	7.84	0.40	0	67	67	M	N-X-N	17	1896	0	0	ZERO	ZERO
P58	81.62	0.27	0.07	0	72	59	M	N-X-N	22	1914	0	0	ZERO	ZERO
P5_P	196.49	24.31	8.22	8.01	25	81	M	P-P-P	28	1992	6	4	LOW	HIGH
P11_P	120.77	7.25	2.83	0	54	60	M	N-N-N	18	1962	0	0	ZERO	ZERO
P12_P	121.28	21.44	8.05	13.55	37	68	M	P-P-P	18	1998	22	12	HIGH	LOW

TABLE I

CLINICAL DATA (COLUMNS 2 TO 9 AND 15) AND SIMULATION RESULTS (COLUMNS 9 TO 14) FOR THE PATIENTS INCLUDED IN THE STUDY (GREEN ROWS: POSITIVE CLINICAL CASES, RED CELLS: HIGH RISK SIMULATIONS). IN COLUMN VT, FIRST LETTER DEFINES IF THE PATIENT HAS EXPERIENCED VT (P) OR NOT (N); SECOND LETTER IS (X) IF VT INDUCIBILITY WAS NOT ATTEMPTED IN CLINIC; IF IT WAS ATTEMPTED, (P) IF VT WAS SUCCESSFULLY INDUCED AND (N) IF NOT; THIRD LETTER INDICATES (P) IF ANY VT WAS OBTAINED DURING SIMULATIONS AND (N) OTHERWISE. IN COLUMN 'CLINICAL RISK', WE PRESENT THE CLINICAL RISK OF EXPERIENCING VT BASED ON THE TYPE OF VT THAT EACH PATIENT EXPERIENCED OR WAS INDUCED. WE CONSIDER VT EPISODES AS HIGH RISK WHEN THEY WERE IDENTIFIED AS SUSTAINED MONOMORPHIC VT OR POLYMORPHIC VT, LOW RISK WHEN THEY WERE CLASSIFIED AS NON-SUSTAINED VT, AND ZERO RISK WHEN VT WAS NOT EXPERIENCED OR INDUCED. THE REST OF THE COLUMNS ARE EXPLAINED ACROSS THE TEXT WHEN REFERENCED.

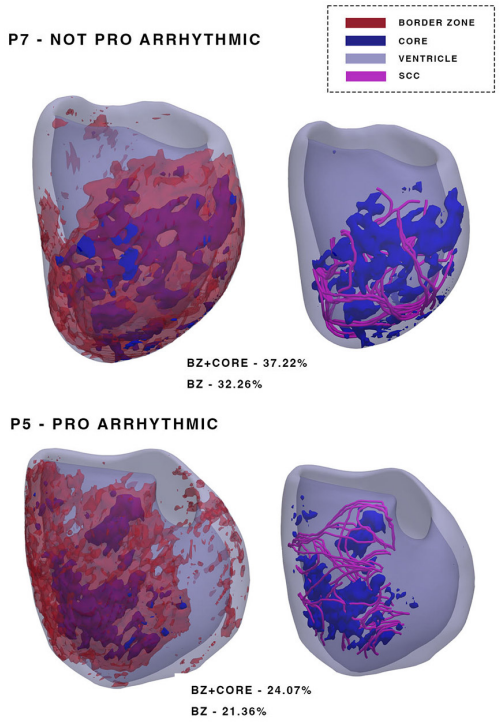

Fig. 2. Segmented models for patients P7 and P5 featuring personalized anatomy, including scar, border Zone, core zone and the extraction of slow conduction channels that extend across the core zone.

locity (CV), whereas repolarization follows an action potential duration (APD) based on a dynamic restitution model. We leverage the event-based computational scheme of fast marching methods [21] to trigger tissue activation with two main benefits: simulation stability, which does not require high resolution spatial and temporal discretizations for convergence, and the absence of a time step, with computation happening only when and where activation and deactivation take place, with a considerable saving in computation effort.

Cell activation follows a phenomenological model with the following variables associated to each node: its activation state (active/inactive), action potential duration (APD), conduction velocity (CV), diastolic interval (DI), and safety factor (SF). The APD and CV vary dynamically according to local DI values, mimicking real myocardial behavior, governed by restitution curves, derived from biophysical simulations based on the ten Tusscher model [22], [23], with values ranging between 200–300ms for APD and between 0.6–0.8m/s for CV in healthy tissue, and ranging between 270–450ms for APD and between 0,015–0,16m/s for CV in border zone. A safety factor-based approach ensures realistic conduction block mechanisms, especially in infarcted tissue regions [24]. Moreover, electrotonic effect and CV memory are considered, defined by a percentage of coupling with neighboring nodes and with previous value, respectively. The values are calibrated to 85% for electrotonic effect and to 5% for CV memory, using data from previous studies [8], [25]. Further details about the electrophysiology solver Arritmic3D, and about the parameter values can be found in [17].

D. Simulation Protocol

We have developed a simulation procedure that replicates and extends the pace-mapping protocol used in electrophysiology labs, covering the entire endocardial and epicardial regions of the LV, including the RV septal wall. In standard VT ablation procedures, stimulation is performed in just a few sites. In our procedure, however, we benefit from the efficiency of the solver to conduct a much more exhaustive study for each patient. During the data pre-processing phase, we automatically define 34 pacing sites, distributed across the 17 AHA segments (17 endocardial sites and 17 epicardial sites) to trigger tissue activation. This approach ensures comprehensive coverage of the spatial relationship between the activation direction and the scar morphology, which plays a significant role in arrhythmia induction.

To account for variability in the parameters for which we do not have patient-specific data, we have varied independently: i) CV in healthy and BZ tissue, adapting the CV Restitution curves by a factor that ranges between 1 and 1.25; ii) APD restitution curves were varied in a range between 0.75 and 1.25, so that differences at the cellular level can also be accounted, see Table II. In each case, the same scaling factor is applied to both healthy and BZ tissue. By automatically combining all detailed parameters, we simulated more than 3600 scenarios per digital twin to assess the potential risk of a VT episode. The ranges were defined so that the parameters remain within physiologically meaning values. Increment size was chosen to trade off between the number of simulations and a proper coverage of the range, taking into account the low sensitivity observed in the activation w.r.t. these parameter values.

Parameter	Initial	Final	Inc	Description
Ectopic	1	34	1	Location of stimuli (AHA Region)
S2 BCL	270	295	5	BCL (ms) for S2 in S1-S2 protocol
#S2	1	3	1	Number of S2 stimuli
CV	1	1.25	0.25	Mult. factor CVR curves
APD	0.75	1.25	0.25	Mult. factor APDR curves

TABLE II

SIMULATION PROTOCOL. FOR EACH PATIENT, 3672 SIMULATIONS ARE PERFORMED BY MODIFYING THE PACING SITE, THE PACING PROTOCOL, APD AND CV. FOR EACH PARAMETER, THE MINIMUM VALUE, THE INCREMENT AND THE MAXIMUM VALUE ARE SHOWN. CV AND APD ARE MODIFIED BY APPLYING A MULTIPLICATION FACTOR TO THE RESTITUTION CURVE, WITH THE SAME SCALING FACTOR APPLIED TO BOTH HEALTHY AND BZ TISSUE.

The following parameters were fixed for all simulations: i) frequency of S1 stimuli (600 ms) as in [26]; ii) the number of S1 stimuli (6) for stabilization; iii) weight of CV memory between consecutive stimuli (5%); and iv) electrotonic effects between neighboring cells (85%). The total simulation time was also fixed to 6000 ms. Note that the construction and execution of the 3600 simulations per digital twin were conducted automatically and continuously, delivering the results for each patient's scenarios immediately upon completion.

For each case, the following results were recorded: the

number of sustained reentries per patient and the associated configurations, including the node ID where the VT initiated, the starting time, the reentry cycle length for at least ten cycles, and the simulation parameters. This allowed us to determine whether positive VT simulations occurred only under extreme parameter values. After the successful completion of the simulations, an automated report was generated for each case, summarizing the results of the simulations.

E. Patient Stratification

We addressed patient stratification in three steps. First, we assessed the complexity of the problem handled from a multiclass classification perspective using clinical biomarkers, in what we called the multiclass baseline scenario. We took the patients annotated by clinicians in three classes (0, 1, 2), where classes 1 and 2 correspond to patients with ventricular tachycardia (VT) stratified into low and high risk, respectively (column *Clinical risk* in Table I), and analyzed the predictive value of clinical biomarkers: LV ejection fraction (LVEF), BZ mass [27], CZ mass [28] and LV mass [29], all of them treated as continuous variables. We incorporated an additional imaging-based metric related to the BZ, the SCC mass, as it has also been reported as predictive of hosting VT isthmuses [30]. This biomarker, however, was assessed separately, since it is less common in clinical practice, to evaluate its predictive power when added to the other biomarkers in this baseline scenario. It is important to note that this multiclass stratification reduces the number of patients in each class, and therefore, the outcomes of this scenario should not be considered statistically robust. Instead, this baseline scenario is included solely to provide insight into the complexity of the clinical criteria classification problem. In this scenario we fitted two models, a decision tree and a random forest, considering a multidimensional input with the different biomarkers, one without SCC and the other with SCC.

Next, we addressed a binary classification problem, by considering LOW and HIGH risk patients as a single RISK class, in opposition to ZERO risk. In this scenario, we fitted one dimensional input classifiers for LVEF, BZ mass, CZ mass and SCC mass separately. We used the same classifiers as in the previous scenario for all of them. This problem was named the baseline binary classification scenario.

Subsequently, we introduced a new metric, named ARRISK, to assess arrhythmia vulnerability by summarizing the simulation results. ARRISK is defined through an index called the AR-index, calculated as the percentage of positive VTs among the effective simulations (column 'Effective sims.' in Table I) for a particular digital twin. Thus, the AR-index is defined in the range 0-100. Once the AR-index was computed, we evaluated its predictive power for clinical diagnosis through a cross-validation process (LOO-nfolds=3) using the same classification models: a decision tree and a random forest. Finally, we defined ARRISK as a digital twin of the clinical diagnosis classes (ZERO/LOW/HIGH); ARRISK is classified as ZERO when the patient's AR-index is 0, LOW when $0 <$ AR-index $\leq \theta$, and HIGH when AR-index $> \theta$, where θ is a threshold that must be estimated.

To have a better insight on the stratification and on the complexity of the classification problem, we used an embedding technique to visualize the classes in the dataset. The T-distributed Stochastic Neighbor Embedding (t-SNE) algorithm was employed to visualize the distribution of patients in a 2D space. t-SNE is a widely used non-linear dimensionality reduction algorithm, that preserves local structure, for visualizing high-dimensional data in lower dimensions, such as two or three dimensions. We applied this technique to obtain a graphical representation of both the ground truth classes and the classes obtained by ARRISK.

F. Clinical follow-up of the cohort

When validating our approach against the clinical data, we face two challenges. On the one hand, the simulation protocol described does not consider the current treatment of real patients. On the other hand, the clinical condition of a patient can change from ZERO to LOW or HIGH if they start suffering from VT, or if VT is induced during a prescribed procedure. For this reason, our stratification is prone to detecting false positives which, in the absence of treatment or after some time, become true positives. To understand the impact of this situation, we conducted a *post hoc* analysis, based on the clinical evolution and treatment of the patients during our study for a period of over two years.

Given that the majority of patients were on beta-blockers, we reviewed the cases predicted as positive by the previous study which were not induced in the clinic. For these cases, a second set of 3600 simulations per case was conducted, incorporating the effect of the beta-blockers to determine if the predicted risk changed. Specifically, the value of APD was increased by a 45%, whereas the CV was reduced a 6%, based on [31], and we revisited the specificity of our predictions under the effect of the medication.

Additionally, the clinical follow-up was used to determine if any cases had experienced a change in their risk level during the study, by the induction of VT in prescribed procedures. For some cases, this clinical follow-up was not possible, due to the inability to induce VT in the clinic. For these cases, *in silico* verification was conducted, using biophysical simulations with the cardiac electrophysiology simulator openCARP [25] using the ten Tusscher model. Each case was remeshed to meet the model's required resolution with an average of 500μm compared to Arritmic3D's 1000μm and a timestep $\Delta t = 0.02ms$. Fiber orientation was incorporated using a Laplace-Dirichlet Rule-Based Method, instead of the Streeter model used by Arritmic3D. To optimize biophysical simulations, only one reentry per case was simulated to verify if pacing from the same zone induces reentry and to confirm if the exit site corresponds.

To obtain reentry results more quickly, the Rapid Pacing method of openCARP was used. This method involves a train of electrical stimulations with a decreasing coupling interval. In this case, the coupling interval was set at 10ms. After the last S1,an S2 stimulus was delivered at a frequency of 370ms. If no reentry occurred, the frequency was decreased to 360 ms, and so on, down to 270 ms. If reentry was still not induced,

an S3 stimulus was added after each S2, following the entire protocol.

III. Results

A. Patient-specific simulation studies

For each of the 51 patients included in the study, a digital twin and computational model were constructed. The set of configurations defined for each digital twin resulted in 3672 3D simulations, which were automatically set up and solved by Arritmic3D.

From this large set of simulations, some did not complete the stimulation protocol. The simulation studies are designed to stress the tissue and assess the risk of arrhythmia, so some configurations fail when attempting to trigger the S2 stimuli. Since each patient has a unique distribution of healthy, border zone and scar tissue, the properties of the stimulation sites, including cell APD and refractory periods, vary, potentially preventing very short coupling intervals. Additionally, if the stimulus is applied to non-excitable tissue (e.g., the scar core zone, CZ), the protocol fails. However, all cases had over 1500 successful simulations, with most achieving around 2000. The number of effective simulations for each case is detailed in Table I.

According to the simulation results, the reentry cycle length (CL) of the VTs ranged from 200 ms to 400 ms, shortening as the reentry became established. Consequently, in positive VT cases, the number of reentry cycles varied between 20 and 30. In our simulation study, 21 patients did not exhibit reentries in any configuration. For cases with reentries, the number of configurations capable of triggering a VT varied between 1 and 36 (See column '#VT' in Table I), In all cases where reentries were observed, except for P28, at least one positive VT was identified using the baseline simulation parameters (discussed in Sec. II-D). This finding suggests that even patients with minimal tissue electrical remodeling may still be at risk. Detailed results for all patients, including the columns '#VT'(simulation results with additional factors applied) and '#VT baseline' (simulation results with baseline parameters applied), are provided in Table I.

For intervention planning, identifying the reentry exit site is crucial. The key question is whether the different exit sites observed in a single case converge on a common region of the heart, representing the physiological exit site, or if they are highly dependent on the simulation configuration. Results indicate that, despite the variety of configurations and pacing sites, exit sites consistently appear in just a few regions. Although the observed VTs may correspond to different circuits, the exit sites tend to cluster into two or three large risk zone groups. This is illustrated in Fig. 3, which is based on AHA segment information and contains data from 20 patients. More precise visualizations of these zones were generated for all cases. Some examples are shown in Fig. 4 for six patients, where each reentry from the 3,000 simulations per case is displayed. The figure highlights the exit site nodes (magenta squares) and the initial stimulation nodes (yellow stars), emphasizing the clustering of risk zones. The simulation results also reveal that not all the pacing sites are equally represented in the reentrant configurations. We found that, out of the 34 pacing points distributed across the ventricle, reentries were generated only at sites located in the peri-infarct zone.

Fig. 5 provides a closer view of the anatomy of patient P5, highlighting the scar and SCCs. In this case, which presents a large number of SCCs, only a portion of the 1830 simulations generated reentries, but all were localized within the same risk zone. In the figure, the SCCs located around the exit sites are circled in blue. This patient-specific identification of localized risk zones is clinically relevant, as these areas are potential candidates for ablation.

B. Baseline Risk Stratification

The results for the multiclass baseline case indicate that we are facing a challenging separability problem, on an unbalanced dataset with a limited number of samples and features (Table III). In the classifier that does not include the SCC mass, the results show that random forest achieves the highest accuracy (76%), but with a slightly lower F1-score (0.49) than the decision tree (0.52). An inspection of the decision tree confirms that the dataset is not easily separable, as both branches of the tree contain nodes representing both classes, requiring up to five levels to cover a six-dimensional dataset. When adding the SCC mass we observed an increase of accuracy, especially for the random forest. This points towards the potential value of SCC mass, which is often overlooked in traditional classification approaches.

Scenario	Model	Accuracy		F1	
		mean	std	mean	std
Baseline without SCC	D.Tree	0.6474	0.1373	0.5203	0.0486
	R.Forest	0.7660	0.0917	0.4912	0.0649
Baseline with SCC	D.Tree	0.6683	0.1448	0.4875	0.0582
	R.Forest	0.8045	0.0650	0.5191	0.0539

TABLE III
CLASSIFICATION RESULTS (CROSS VALIDATION) OBTAINED FROM THE DATASET USING THE DIFFERENT CLINICAL CRITERIA IN A SINGLE CLASSIFIER. THE RESULTS ARE PRESENTED FOR THE MODELS FITTED WITHOUT THE SCC MASS AND WITH THE SCC MASS. RESULTS WERE OBTAINED WITH 3-FOLD CROSS VALIDATION.

By inspecting the classification based on AR-index we find 13 true positives, 10 true negatives, 17 false positives, and 1 false negative, resulting in a high sensitivity of 0.93 and a relatively low specificity of 0.54. For the random forest classifiers (which is the model that yields the best results) in the baseline binary classification scenario, the ROC curves are presented in Fig. 6, allowing for a direct comparison of their performance. The AR-index-based classifier performs competitively, with an area under the curve (AUC) of 0.74, comparable to LVEF, with AUC of 0.79. In comparison, the AR-index leverages valuable complementary information, in the sense that it is able to provide simulation-based insights on risk assessment that are not directly available from raw imaging data analysis.

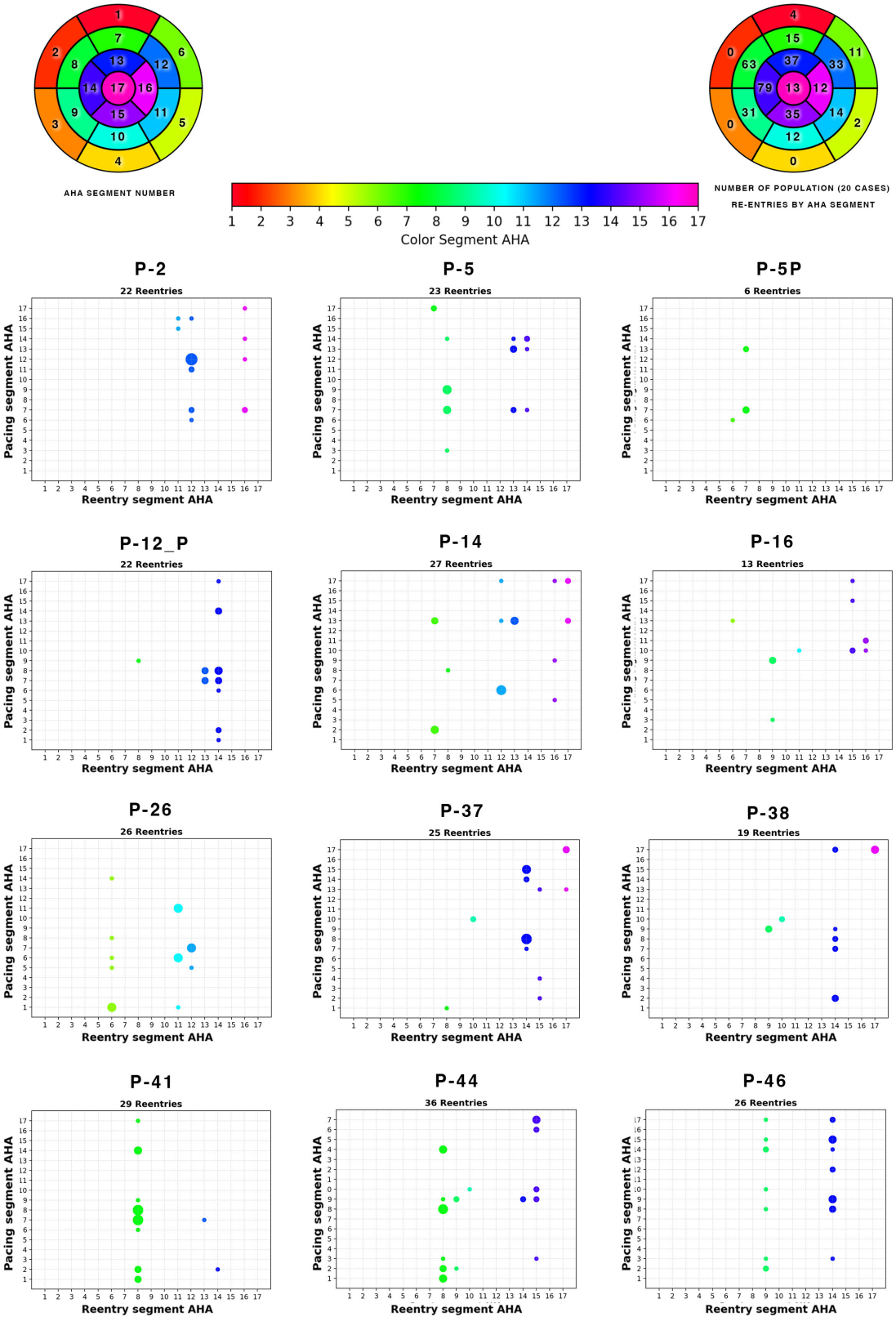

Fig. 3. Results from various example cases, showing all simulations where VT could be induced. Each case displays on the x-axis the exit sites that initiate the reentries, with points colored according to the AHA segment they belong to. The bullseye legend, shown in the top left corner, illustrates the colors assigned to each segment. On the y-axis, the AHA segment from which pacing was performed in that induced reentry is detailed, with the size of the point increasing if different reentries occur from the same pacing AHA segment. In the top right corner, a bullseye chart shows the cumulative sum of simulations with induced VT in each AHA segment across all 20 positive cases.

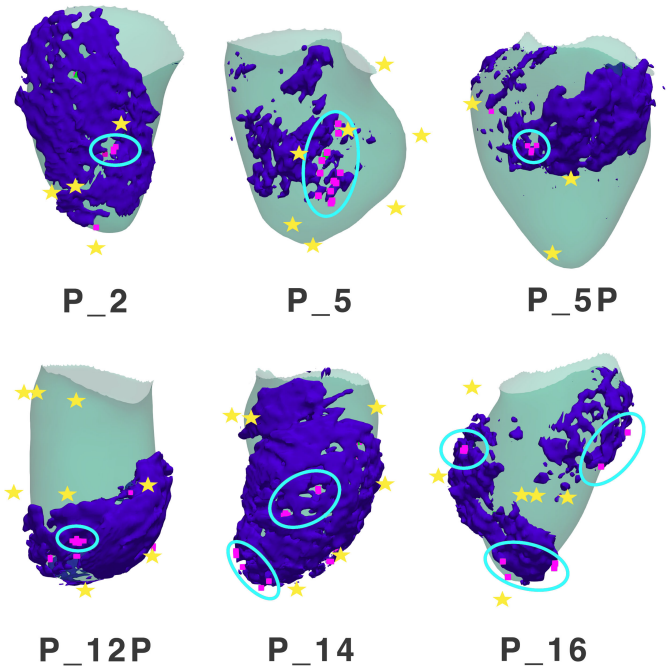

Fig. 4. Results across multiple example cases, showing all simulations where ventricular tachycardia was induced, visualized on the ventricle of each case. The core zone is depicted in purple. Yellow stars indicate pacing sites, whereas magenta squares represent the scar exit sites where ventricular tachycardia was initiated. Blue circles highlight areas where exit points frequently cluster around specific hot spots. Despite the reentries being triggered from various pacing sites and parameter configurations, the exit sites consistently cluster in only a few regions.

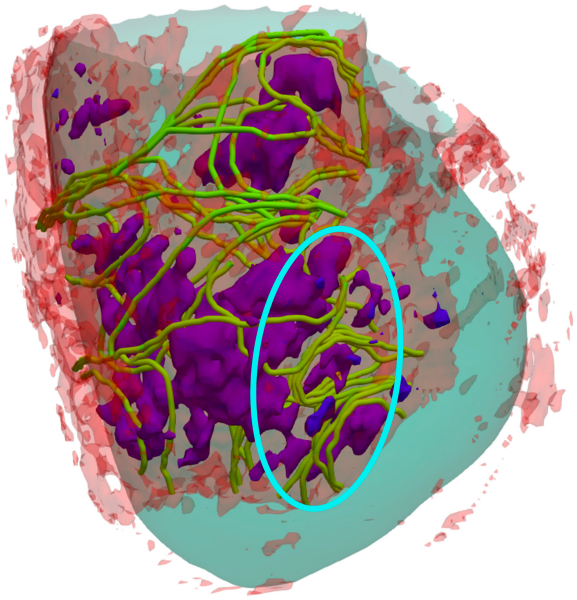

Fig. 5. Detail of the phenotype of patient P5. The border zone is shown in red, the core zone in purple, and the slow conduction channels in green. The blue circle highlights the high-risk slow conduction channels that correspond with the results shown in Fig. 4.

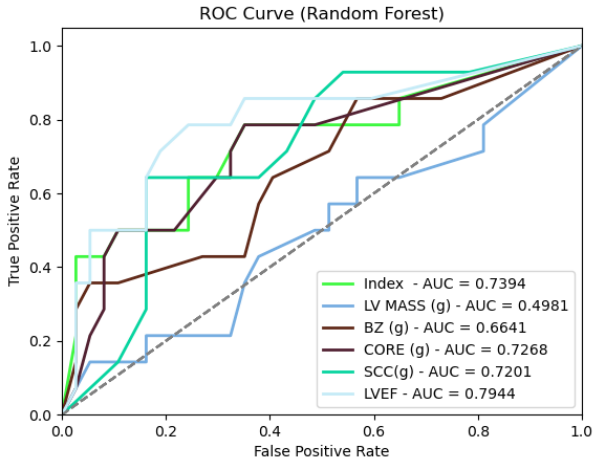

Fig. 6. ROC curves for the different one dimensional random forest classifiers.

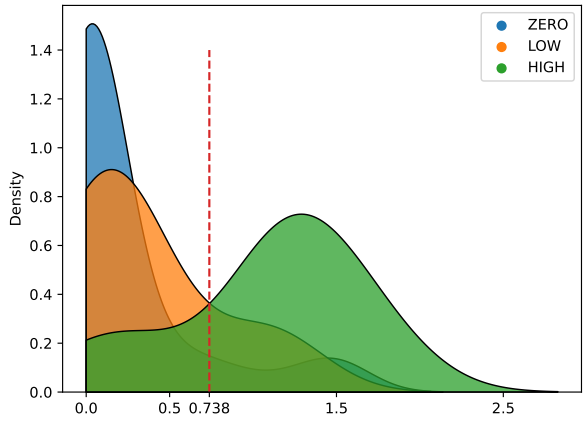

Fig. 7. AR-index distributions derived from the clinical diagnosis classes (probability density curves). The value $\mathbf{0.738}$ has been selected as the threshold ($\boldsymbol{\theta}$), required by the ARRISK method to separate the 3 classes defined for this stratification problem.

C. ARRISK-based Risk Stratification

Next, we present the results obtained from the computation of ARRISK for patient stratification among three groups based on VT type (ZERO, LOW, HIGH). Fig. 7 shows the distributions of the AR-index for these three groups of patients. Note that, as it can be observed in column #VT of Table I, the number of simulations that induce an arrhythmia is in the order of dozens, being the AR-index always below 2%. For this dataset, the optimal stratification results are achieved with an AR-index threshold of $\theta = 0.738$, which corresponds to the exact point where the distributions of the LOW and HIGH patient groups intersect.

The new ARRISK-based stratification was consistent with the clinical results in the majority of true (clinical) positive cases. However, as expected, clinically negative cases exhibited different behavior, with a notable number of apparent false positives.

For 17 of the 37 negative cases in Table I, ARRISK predicted LOW or HIGH risk. These cases had not undergone VT induction attempts and they were on beta-blockers. as part of their therapy, which likely caused a mismatch between the patients' clinical conditions and the simulations, as the simulations were conducted in the absence of any treatment. Simulations of these 17 clinically negative cases with LOW and HIGH ARRISK scores were repeated following the methodology discussed in Sec. II-F, incorporating the effects of beta-blockers. In Table IV, it can be observed that after accounting for the effect of beta-blockers, most cases with a LOW ARRISK score shifted to ZERO risk. However, cases with HIGH ARRISK scores continued to present nonzero risk, with the majority still classified as HIGH. All 17 cases were clinically negative, but VT induction was not performed in the clinic, except for case 38, which had a negative outcome. Notably, this case's ARRISK score changed from HIGH to LOW after simulating the effect of beta-blockers.

PATIENT	Clinical Risk	ARRISK	ARRISK with beta-blockers
P4	ZERO	LOW	ZERO
P7	ZERO	LOW	LOW
P9	ZERO	LOW	ZERO
P10	ZERO	LOW	ZERO
P14	ZERO	HIGH	HIGH
P16	ZERO	LOW	LOW
P21	ZERO	LOW	ZERO
P24	ZERO	LOW	ZERO
P26	ZERO	HIGH	HIGH
P28	ZERO	LOW	ZERO
P29	ZERO	LOW	ZERO
P32	ZERO	LOW	ZERO
P33	ZERO	LOW	ZERO
P35	ZERO	LOW	ZERO
P36	ZERO	LOW	ZERO
P38	ZERO	HIGH	LOW
P41	ZERO	HIGH	HIGH

TABLE IV

SIMULATIONS WITH THE EFFECT OF BETA-BLOCKERS, IN CLINICALLY NEGATIVE CASES WITH POSITIVE RESULTS IN THE INITIAL SIMULATIONS OF THE STUDY. ROWS SHADED IN GREED CORRESPOND TO POSITIVE CASES WITH BETA-BLOCKER EFFECT. NONE OF THE PATIENTS IN THIS TABLE WERE INDUCED VT IN THE CLINIC EXCEPT FOR CASE P38, WHICH GAVE NEGATIVE RESULT. MOST OF THE PATIENTS WITH LOW ARRISK SCORE CHANGED TO ZERO AFTER SIMULATING THE EFFECT OF BETA-BLOCKERS.

Another noteworthy fact is that three of the cases that are reflected as positive in Table I were, by the start of our study, negative, whereas they were predicted as RISK patients by ARRISK. After updating their clinical history, patients 18, 45 and 53 were reported as positive; patient P18 experienced a NSVT, and patients P45 and P53 had undergone VT induction attempts, both resulting in SMVT.

D. t-SNE Projection of Patients

Fig. 8 presents the t-SNE analysis for both the ground truth stratification and the ARRISK stratification. It is important to note that t-SNE performs a nonlinear projection from high-dimensional space to low-dimension space (2D in our case) to visually separate clusters. In this projection, the axes do not correspond to any variable in the original data and are unitless. The left plot shows the analysis for the clinical stratification (ground truth). In this case, positive patients (red color) tend to be cluster in the upper right corner, whereas the negative patients (blue color) are more dispersed across the space, with a slight tendency to concentrate in the lower left area. Both classes are highly intermixed, indicating that it will be challenging to establish a simple criterion to separate them.

Fig. 8, right, shows the t-SNE projection of the patients, focusing on their positive and negative classification according to ARRISK, and comparing it to the clinical risk outcome. The color in the center of each point represents the ARRISK class, whereas the border color corresponds to the clinical class of the dataset. The three clinical cases that changed from negative to positive labels after follow-up have been updated in this graph compared to Fig. 8, left. Among the clinically positive cases (red and pink), ARRISK coincides in 13 out of 14 cases, with the risk level matching in 77% of these 13 cases. Only one clinically positive case with LOW risk is classified as negative. Regarding negative cases (blue), ARRISK matches the clinical result in 20 out of 37 cases, distributing the risk among the 17 non-matching cases, with 13 classified as LOW risk and 4 as HIGH risk.

These 4 cases can be identified in Fig. 8 by a blue border with a red inner circle. Case P14 is positioned near positive neighboring cases, whereas cases P41, P38, and P26 are situated closer to negative neighbors. Consequently, these cases present greater difficulty in stratification based solely on pre-simulation data.

In Table V, we present the Arritmic3D results for these HIGH-risk cases. The table specifies the AHA segment from which pacing was applied (Pacing site), the AHA segment where the reentry initiated (Exit site), and the Cycle Length of the reentry. All cases correspond to sustained ventricular tachycardia.

	Arritmic3D		
Case	AHA stim	AHA exit	CL
P14	13	7/13	S4 - 295
P26	7	12	S4 - 290
P38	9	9	S4 - 280
P41	7	8	S4 - 290

TABLE V

REENTRY INFORMATION FOR 4 HIGH-RISK CASES SELECTED FOR FURTHER VERIFICATION OF PACING SITE AND EXIT SITE USING OPENCARP. THE INFORMATION IN THIS TABLE CORRESPONDS TO THE RESULTS OBTAINED WITH ARRITMIC3D. ALL REENTRIES CORRESPOND TO SUSTAINED VENTRICULAR TACHYCARDIA. AHA STIM: AHA SEGMENT USED FOR STIMULATION; AHA EXIT: AHA SEGMENT WHERE EXIT TOOK PLACE; CL: CYCLE LENGTH REENTRY.

E. Biophysical Simulation of High-Risk Cases

For the verification of these 4 HIGH-risk cases, biophysical simulations were conducted using the cardiac electrophysiology simulator openCARP. Table VI presents the results obtained with openCARP. Reentries were successfully induced in all 4 cases by stimulating from the same pacing zone, and

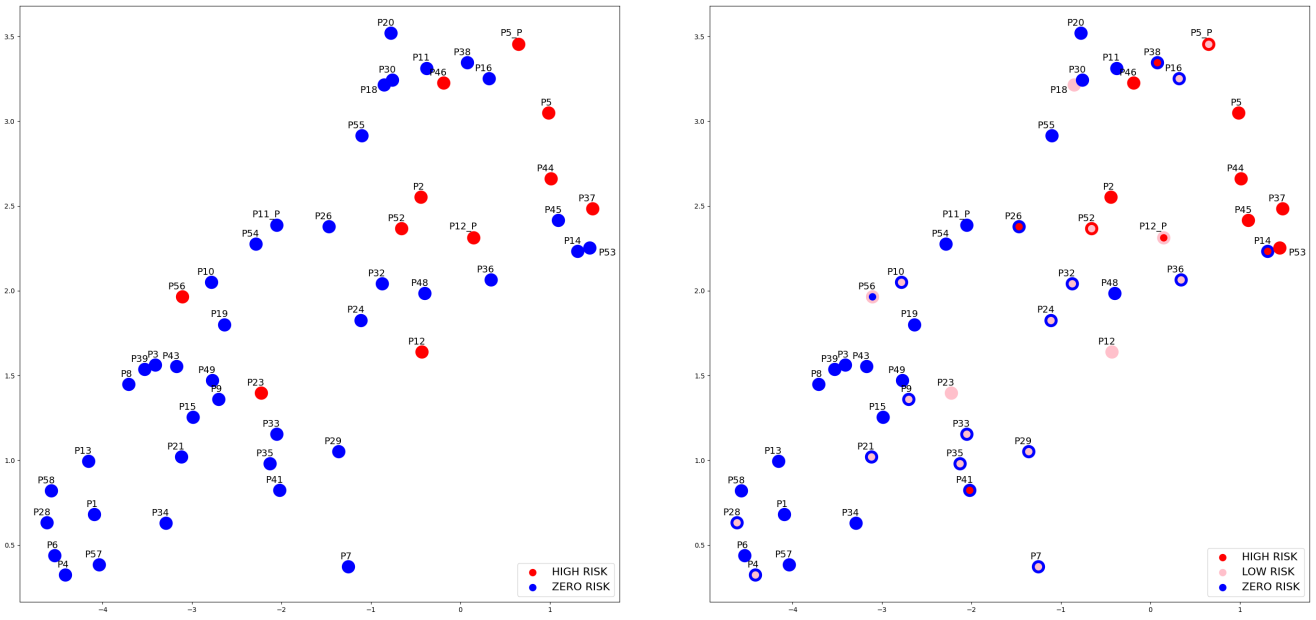

Fig. 8. Left: Visualization of the patient dataset using t-SNE. The color of each point indicates the clinical classification of the patient (red: HIGH risk, blue: ZERO risk). The scale of the axes is derived from the t-SNE projection and does not correspond to the original feature space. Right: ARRISK performance on the 51-case dataset. The outer border represents clinical risk, whereas the inner circle denotes the ARRISK score (red: HIGH risk, pink: LOW risk, blue: ZERO risk).

the initiation site of the reentry was consistent across cases. Additionally, the cycle length of the reentries showed minor differences, with variations of up to 10 ms at most. In all cases, the outcome was also a sustained ventricular tachycardia, in agreement with Arritmic3D results. These findings confirm the accuracy of the reentries obtained and the risk zones detected by Arritmic3D.

Biophysical Simulations - openCARP			
Case	AHA stim	AHA exit	CL
P14	13	7/13	S2 - 310
P26	7	12	S2 - 310
P38	9	9	S2 - 280
P41	7	8	S2 - 290

TABLE VI

RESULTS OF IN SILICO PACING USING OPENCARP BIOPHYSICAL SOLVER, USING THE SAME PACING SITE USED WITH ARRITMIC3D. AS IN TABLE V, ALL CASES PRESENT SUSTAINED VENTRICULAR TACHYCARDIA. AHA STIM: AHA SEGMENT USED FOR STIMULATION; AHA EXIT: AHA SEGMENT WHERE EXIT TOOK PLACE; CL: CYCLE LENGTH REENTRY.

We find good agreement between clinical results and the ARRISK score where the clinical classification is more conclusive, whereas cases where ARRISK might be considered to fail could still have their classification in clinical history. Moreover, among the 17 non-matching negative cases, ARRISK returned 13 LOW-risk scores, and 11 of these changed to ZERO when beta-blockers were simulated. For further insight, Fig. 9 presents a comparison between the biophysical simulations with openCARP and Arritmic3D for one of the reentries obtained from case P41, highlighting the previously noted similarities.

IV. DISCUSSION

The results presented in Fig. 8 demonstrate a strong concordance between the proposed ARRISK score and clinical labeling, especially in positive cases—HIGH risk (red) and LOW risk (pink)—and negative cases. However, notable discrepancies were observed in negative clinical cases, where several LOW and HIGH-risk scores were assigned by ARRISK. Interestingly, only in three of these cases (P38, P48, P11_P) were attempts made to induce VTs clinically. For these three cases, ARRISK aligned with the negative result in P48 and P11_P, where no reentries were induced by septal wall stimulation, as performed by the medical team. In case P38, despite negative clinical inducibility, our simulations still indicated a reentry risk, as discussed in Sec. III-D. For the remaining cases, no inducibility test was conducted, and these patients were under beta-blocker therapy, which may have influenced their clinical status.

The ability to perform a large number of simulations with varied parameters and model configurations also allowed us to assess the stability of the ARRISK score. Expanding restitution curve ranges yielded consistent VT reentries, as shown in Table I. When reentries are found with the baseline set of parameters obtained from the ten Tusscher model (column '#VT baseline' in Table I), they are also found in simulations with expanded CV (1.0–1.25) and APD (0.75–1.25) ranges (column '#VT'). The agreement between these columns indicates that patient stratification is robust to variations in restitution curve values. This is critical for identifying highly proarrhythmic cases. This approach is consistent with the findings of Deng et al. [10] and Prakosa et al. [12], who noted that regions with dense scar tissue and slow conduction channels are more likely to sustain reentrant circuits, particularly when these

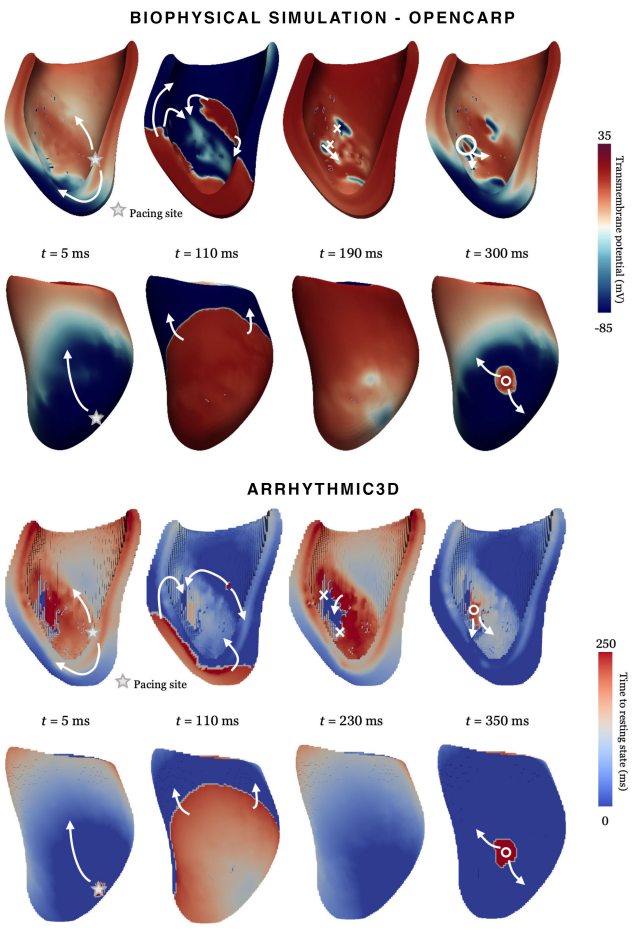

Fig. 9. Comparison of ventricular tachycardia initiation in case P41. (Top) Biophysical simulation with openCARP, (Bottom) Simulation with Arritmic3D. In each simulation, the snapshots correspond to the posterior view (top) and the anterior view (bottom) of the left ventricle. The time instant above each map is measured from the delivery of the last pacing stimulus. White arrows indicate the direction of propagation, white crosses mark propagation blocks. The gray star denotes the initial pacing site, and the white circle represents the initial exit site of the reentry.

regions consistently produce reentries under varied simulation conditions.

The robustness of ARRISK is further evidenced by our observation that if a scar area can reproduce the same reentry with different simulation parameters, it is more likely to generate reentries compared to scars that produce reentries only under a specific set of conditions. This insight is consistent with the work of Arevalo et al. [26], who developed the VARP index to assess the risk of sudden cardiac death (SCD) using multi-site pacing and biophysical simulations. They found that patients whose models could trigger VT from multiple pacing locations were at a higher risk of SCD. Our study extends this concept by incorporating a larger number of pacing sites (34 compared to 19 in Arevalo et al.'s study) and by varying additional tissue properties such as CVR and APDR, further enhancing the predictive accuracy of the model.

Reentry generation conditions include specific ranges of conduction velocity (CV: 1.0–1.25) and action potential duration (APD: 0.75–1.25) values, with pacing in the peri-infarct zone significantly contributing to reentry clustering. These conditions were identified through extensive simulations that systematically varied CV and APD parameters within physiologically plausible ranges. The robustness of reentry generation across these parameter ranges aligns with uncertainty quantification practices, ensuring that our findings are not overly dependent on a single set of conditions. Specifically, scars that consistently produce reentries under a wide range of CV and APD values are more likely to sustain arrhythmias compared to those that only produce reentries under highly specific conditions. This variability in reentry susceptibility reflects the heterogeneous nature of scar tissue and its interaction with surrounding healthy tissue, as highlighted in prior studies.

Our findings align with Sung et al. [32], [33], who emphasized the importance of the interaction between scar morphology and conduction properties in arrhythmia formation. Our results confirm that SCCs significantly contribute to the generation and maintenance of VTs. However, we observed that not all large SCC masses are associated with a high risk of reentry, highlighting the need to consider the specific morphological relationship between the BZ and CZ. This nuance was also noted by Sung et al., who pointed out that complex scar geometries, especially those involving intricate SCC networks, require detailed analysis to accurately assess arrhythmic risk.

Moreover, our methodology, which allows for the simulation of thousands of scenarios within a single day, represents a significant advancement toward bridging the gap between in-silico studies and clinical practice. As Xie et al. [34] argued, computational approaches like ARRISK could be integrated into clinical workflows to provide real-time risk assessments, thereby enabling more timely and targeted interventions. Our system's ability to provide a comprehensive risk assessment, including the identification of potential ablation sites, within such a short time frame underscores its practical applicability in clinical settings.

The validation of our results through biophysical simulations using openCARP further strengthens the credibility of our approach. Okada et al. [35] highlighted the importance of validating computational predictions with detailed biophysical models to ensure their clinical relevance. In our study, the agreement between the reentries and risk zones detected by ARRISK and those confirmed by openCARP simulations demonstrates the reliability of our method. This validation step is crucial for ensuring that the insights gained from ARRISK are not only theoretically sound but also applicable in real-world clinical scenarios.

The size of the cohort does not allow us to raise strong conclusions from a clinical perspective. However, the findings of this study indicate that, upon further validation, ARISK can become a useful biomarker. Our *post hoc* study on beta-blockers and the apparent false positives which, during the study, become true positives are in concordance with prior studies, such as those by Zhou et al. [36] and Trayanova et al. [37], which emphasize the potential of computational models to uncover latent arrhythmic risks not detectable by

standard clinical procedures. Comparing our findings with the work of Aronis et al. [38], who demonstrated the power of patient-specific models in predicting arrhythmic events, we see a consistent pattern where computational models provide insights beyond traditional imaging and electrophysiological tests.

While the dataset consists of 51 patients, it aligns with comparable studies in the field [10], [36], [39]. Furthermore, the strong concordance between ARRISK predictions and clinical outcomes supports the robustness of our findings. Future work aims to validate these findings on larger, multi-center cohorts to enhance generalizability.

A limitation of our study is the usage of fixed thresholds to segment CZ, BZ and SCC. Sensitivity to segmentation parameters and to different readers should be done to ensure the robustness of our findings and enhance its clinical applicability. The Arritmic3D solver is specially suited for such an analysis, since it enables the execution of thousands of simulations in minutes, as it has been demonstrated in this study. This sensitivity analysis is left as future work.

Another limitation is that, in its current implementation, Arritmic3D cannot account for non zero CV in the scar CZ. While this assumption is often made in the literature, it has been observed experimentally that pacing in very dense scar zones can produce activations [40]. Future evolutions of the solver will consider the inclusion of this feature as one of the development lines.

In summary, the ARRISK score, supported by extensive computational simulations and validated through biophysical modeling, offers a promising tool for improving the stratification and management of patients at risk of ventricular tachycardia. By integrating advanced computational models with clinical data, we can enhance the accuracy of arrhythmic risk predictions, leading to better-informed decisions regarding patient management. This approach aligns with the broader trend in precision medicine, where tailored treatments based on individual risk profiles are increasingly recognized as the key to improving outcomes in complex cardiac conditions.

V. Conclusions

In this study, we introduced the ARRISK score, a computational tool designed to enhance the stratification and management of patients at risk of ventricular tachycardia (VT). Through extensive simulations incorporating a wide range of electrophysiological parameters, ARRISK demonstrated strong concordance with clinical outcomes, particularly in identifying high-risk patients. Our findings underscore the value of integrating computational models with clinical data to provide a more comprehensive assessment of arrhythmic risk. The validation of our approach through biophysical simulations further supports the clinical applicability of ARRISK. This tool represents a significant step toward more personalized and precise treatment strategies in cardiac care, ultimately contributing to improved patient outcomes.

References

[1] A.-C. Pouleur, E. Barkoudah, H. Uno, H. Skali, P. V. Finn, S. L. Zelenkofske, Y. N. Belenkov, V. Mareev, E. J. Velazquez, J. L. Rouleau, A. P. Maggioni, L. Køber, R. M. Califf, J. J. V. McMurray, M. A. Pfeffer, S. D. Solomon, and VALIANT Investigators, "Pathogenesis of sudden unexpected death in a clinical trial of patients with myocardial infarction and left ventricular dysfunction, heart failure, or both," *Circulation*, vol. 122, no. 6, pp. 597–602, Aug 2010.

[2] J. K. Donahue, J. Chrispin, and O. A. Ajijola, "Mechanism of ventricular tachycardia occurring in chronic myocardial infarction scar," *Circ Res*, vol. 134, no. 3, pp. 328–342, Feb 2024.

[3] W. G. Stevenson, P. L. Friedman, D. Kocovic, P. T. Sager, L. A. Saxon, and B. Pavri, "Radiofrequency catheter ablation of ventricular tachycardia after myocardial infarction," *Circulation*, vol. 98, no. 4, pp. 308–314, 1998.

[4] E. M. Cronin, F. M. Bogun, P. Maury, P. Peichl, M. Chen, N. Namboodiri, L. Aguinaga, L. R. Leite, S. M. Al-Khatib, E. Anter, A. Berruezo, D. J. Callans, M. K. Chung, P. Cuculich, A. d'Avila, B. J. Deal, P. D. Bella, T. Deneke, T.-M. Dickfeld, C. Hadid, H. M. Haqqani, G. N. Kay, R. Latchamsetty, F. Marchlinski, J. M. Miller, A. Nogami, A. R. Patel, R. K. Pathak, L. C. Saenz Morales, P. Santangeli, J. L. Sapp, Jr, A. Sarkozy, K. Soejima, W. G. Stevenson, U. B. Tedrow, W. S. Tzou, N. Varma, and K. Zeppenfeld, "2019 hrs/ehra/aphrs/lahrs expert consensus statement on catheter ablation of ventricular arrhythmias: Executive summary," *J Arrhythm*, vol. 36, no. 1, pp. 1–58, Feb 2020.

[5] N. A. Trayanova and A. Prakosa, "Up digital and personal: How heart digital twins can transform heart patient care," *Heart Rhythm*, vol. 21, no. 1, pp. 89–99, Jan 2024.

[6] J. Corral-Acero, F. Margara, M. Marciniak, C. Rodero, F. Loncaric, Y. Feng, A. Gilbert, J. F. Fernandes, H. A. Bukhari, A. Wajdan, M. V. Martinez, M. S. Santos, M. Shamohammdi, H. Luo, P. Westphal, P. Leeson, P. DiAchille, V. Gurev, M. Mayr, L. Geris, P. Pathmanathan, T. Morrison, R. Cornelussen, F. Prinzen, T. Delhaas, A. Doltra, M. Sitges, E. J. Vigmond, E. Zacur, V. Grau, B. Rodriguez, E. W. Remme, S. Niederer, P. Mortier, K. McLeod, M. Potse, E. Pueyo, A. Bueno-Orovio, and P. Lamata, "The 'digital twin' to enable the vision of precision cardiology," *Eur Heart J*, vol. 41, no. 48, pp. 4556–4564, Dec 2020.

[7] K. H. Ten Tusscher, R. Hren, and A. V. Panfilov, "Organization of ventricular fibrillation in the human heart," *Circulation research*, vol. 100, no. 12, pp. e87–e101, 2007.

[8] S. A. Niederer, E. Kerfoot, A. P. Benson, M. O. Bernabeu, O. Bernus, C. Bradley, E. M. Cherry, R. Clayton, F. H. Fenton, A. Garny, E. Heidenreich, S. Land, M. Maleckar, P. Pathmanathan, G. Plank, J. F. Rodríguez, I. Roy, F. B. Sachse, G. Seemann, O. Skavhaug, and N. P. Smith, "Verification of cardiac tissue electrophysiology simulators using an N-version benchmark," *Philos Trans A Math Phys Eng Sci*, vol. 369, no. 1954, pp. 4331–51, Nov 2011.

[9] Z. Chen, R. Cabrera-Lozoya, J. Relan, M. Sohal, A. Shetty, R. Karim, H. Delingette, J. Gill, K. Rhode, N. Ayache, P. Taggart, C. A. Rinaldi, M. Sermesant, and R. Razavi, "Biophysical modeling predicts ventricular tachycardia inducibility and circuit morphology: A combined clinical validation and computer modeling approach," *J Cardiovasc Electrophysiol*, vol. 27, no. 7, pp. 851–60, 07 2016.

[10] D. Deng, A. Prakosa, J. Shade, P. Nikolov, and N. A. Trayanova, "Characterizing conduction channels in postinfarction patients using a personalized virtual heart," *Biophys J*, vol. 117, no. 12, pp. 2287–2294, 12 2019.

[11] A. Lopez-Perez, R. Sebastian, M. Izquierdo, R. Ruiz, M. Bishop, and J. M. Ferrero, "Personalized cardiac computational models: From clinical data to simulation of infarct-related ventricular tachycardia," *Front Physiol*, vol. 10, p. 580, 2019.

[12] A. Prakosa, H. J. Arevalo, D. Deng, P. M. Boyle, P. P. Nikolov, H. Ashikaga, J. J. E. Blauer, E. Ghafoori, C. J. Park, R. C. Blake, 3rd, F. T. Han, R. S. MacLeod, H. R. Halperin, D. J. Callans, R. Ranjan, J. Chrispin, S. Nazarian, and N. A. Trayanova, "Personalized virtual-heart technology for guiding the ablation of infarct-related ventricular tachycardia," *Nat Biomed Eng*, vol. 2, no. 10, pp. 732–740, Oct 2018.

[13] Y. Zhang, K. Zhang, A. Prakosa, C. James, S. L. Zimmerman, R. Carrick, E. Sung, A. Gasperetti, C. Tichnell, B. Murray, H. Calkins, and N. A. Trayanova, "Predicting ventricular tachycardia circuits in patients with arrhythmogenic right ventricular cardiomyopathy using genotype-specific heart digital twins," *Elife*, vol. 12, Oct 2023.

[14] P. Bhagirath, F. O. Campos, P. Postema, M. J. B. Kemme, A. A. M. Wilde, A. J. Prassl, A. Neic, C. A. Rinaldi, M. J. W. Götte, G. Plank, and M. J. Bishop, "Arrhythmogenic vulnerability of re-entrant pathways in post-infarct ventricular tachycardia assessed by advanced computational modelling," *Europace*, vol. 25, no. 9, Aug 2023.

[15] A. Loewe, E. Poremba, T. Oesterlein, A. Luik, C. Schmitt, G. Seemann, and O. Dössel, "Patient-specific identification of atrial flutter

vulnerability-a computational approach to reveal latent reentry pathways," *Front Physiol*, vol. 9, p. 1910, 2018.

[16] A. Neic, F. O. Campos, A. J. Prassl, S. A. Niederer, M. J. Bishop, E. J. Vigmond, and G. Plank, "Efficient computation of electrograms and ecgs in human whole heart simulations using a reaction-eikonal model," *J Comput Phys*, vol. 346, pp. 191–211, Oct 2017.

[17] D. Serra, P. Romero, I. Garcia-Fernandez, M. Lozano, A. Liberos, M. Rodrigo, A. Bueno-Orovio, A. Berruezo, and R. Sebastian, "An automata-based cardiac electrophysiology simulator to assess arrhythmia inducibility," *Mathematics*, vol. 10, no. 8, p. 1293, 2022.

[18] C. Mendonca Costa, P. Gemmell, M. K. Elliott, J. Whitaker, F. O. Campos, M. Strocchi, A. Neic, K. Gillette, E. Vigmond, G. Plank, R. Razavi, M. O'Neill, C. A. Rinaldi, and M. J. Bishop, "Determining anatomical and electrophysiological detail requirements for computational ventricular models of porcine myocardial infarction," *Comput Biol Med*, vol. 141, p. 105061, Nov 2021.

[19] A. Lopez-Perez, R. Sebastian, and J. M. Ferrero, "Three-dimensional cardiac computational modelling: methods, features and applications," *Biomed Eng Online*, vol. 14, p. 35, Apr 2015.

[20] D. D. Streeter Jr, H. M. Spotnitz, D. P. Patel, J. Ross Jr, and E. H. Sonnenblick, "Fiber orientation in the canine left ventricle during diastole and systole," *Circulation research*, vol. 24, no. 3, pp. 339–347, 1969.

[21] J. A. Sethian, "Fast marching methods," *SIAM Review*, vol. 41, no. 2, pp. 199–235, 1999. [Online]. Available: https://doi.org/10.1137/S0036144598347059

[22] K. H. W. J. ten Tusscher, D. Noble, P. J. Noble, and A. V. Panfilov, "A model for human ventricular tissue," *Am J Physiol Heart Circ Physiol*, vol. 286, no. 4, pp. H1573–89, Apr 2004.

[23] K. H. T. Tusscher and A. V. Panfilov, "Cell model for efficient simulation of wave propagation in human ventricular tissue under normal and pathological conditions." *Phys Med Biol*, vol. 51, no. 23, pp. 6141–6156, Dec 2006.

[24] P. M. Boyle, W. H. Franceschi, M. Constantin, C. Hawks, T. Desplantez, N. A. Trayanova, and E. J. Vigmond, "New insights on the cardiac safety factor: Unraveling the relationship between conduction velocity and robustness of propagation," *J Mol Cell Cardiol*, vol. 128, pp. 117–128, 03 2019.

[25] G. Plank, A. Loewe, A. Neic, C. Augustin, Y.-L. Huang, M. A. Gsell, E. Karabelas, M. Nothstein, A. J. Prassl, J. Sánchez *et al.*, "The opencarp simulation environment for cardiac electrophysiology," *Computer methods and Programs in Biomedicine*, vol. 208, p. 106223, 2021.

[26] H. J. Arevalo, F. Vadakkumpadan, E. Guallar, A. Jebb, P. Malamas, K. C. Wu, and N. A. Trayanova, "Arrhythmia risk stratification of patients after myocardial infarction using personalized heart models," *Nat Commun*, vol. 7, p. 11437, 05 2016.

[27] S. D. Roes, C. J. W. Borleffs, R. J. van der Geest, J. J. M. Westenberg, N. A. Marsan, T. A. M. Kaandorp, J. H. C. Reiber, K. Zeppenfeld, H. J. Lamb, A. de Roos, M. J. Schalij, and J. J. Bax, "Infarct tissue heterogeneity assessed with contrast-enhanced mri predicts spontaneous ventricular arrhythmia in patients with ischemic cardiomyopathy and implantable cardioverter-defibrillator," *Circ Cardiovasc Imaging*, vol. 2, no. 3, pp. 183–90, May 2009.

[28] I. Klem, J. W. Weinsaft, T. D. Bahnson, D. Hegland, H. W. Kim, B. Hayes, M. A. Parker, R. M. Judd, and R. J. Kim, "Assessment of myocardial scarring improves risk stratification in patients evaluated for cardiac defibrillator implantation," *J Am Coll Cardiol*, vol. 60, no. 5, pp. 408–20, Jul 2012.

[29] K. Reinier, C. Dervan, T. Singh, A. Uy-Evanado, S. Lai, K. Gunson, J. Jui, and S. S. Chugh, "Increased left ventricular mass and decreased left ventricular systolic function have independent pathways to ventricular arrhythmogenesis in coronary artery disease," *Heart Rhythm*, vol. 8, no. 8, pp. 1177–82, Aug 2011.

[30] M. Takigawa, J. Duchateau, F. Sacher, R. Martin, K. Vlachos, T. Kitamura, M. Sermesant, N. Cedilnik, G. Cheniti, A. Frontera, N. Thompson, C. Martin, G. Massoullie, F. Bourier, A. Lam, M. Wolf, W. Escande, C. André, T. Pambrun, A. Denis, N. Derval, M. Hocini, M. Haissaguerre, H. Cochet, and P. Jaïs, "Are wall thickness channels defined by computed tomography predictive of isthmuses of postinfarction ventricular tachycardia?" *Heart Rhythm*, vol. 16, no. 11, pp. 1661–1668, 11 2019.

[31] R. A. Gray and M. R. Franz, "Amiodarone prevents wave front-tail interactions in patients with heart failure: an in silico study," *American Journal of Physiology-Heart and Circulatory Physiology*, vol. 325, no. 5, pp. H952–H964, 2023.

[32] E. Sung, A. Prakosa, K. N. Aronis, S. Zhou, S. L. Zimmerman, H. Tandri, S. Nazarian, R. D. Berger, J. Chrispin, and N. A. Trayanova, "Personalized digital-heart technology for ventricular tachycardia ablation targeting in hearts with infiltrating adiposity," *Circulation: Arrhythmia and Electrophysiology*, vol. 13, no. 12, p. e008912, 2020.

[33] E. Sung, A. Prakosa, S. Kyranakis, R. D. Berger, J. Chrispin, and N. A. Trayanova, "Wavefront directionality and decremental stimuli synergistically improve identification of ventricular tachycardia substrate: insights from personalized computational heart models," *Europace*, vol. 25, no. 1, pp. 223–235, 2023.

[34] E. Xie, E. Sung, E. Saad, N. Trayanova, K. C. Wu, and J. Chrispin, "Advanced imaging for risk stratification for ventricular arrhythmias and sudden cardiac death," *Frontiers in Cardiovascular Medicine*, vol. 9, p. 884767, 2022.

[35] D. R. Okada, J. Miller, J. Chrispin, A. Prakosa, N. Trayanova, S. Jones, M. Maggioni, and K. C. Wu, "Substrate spatial complexity analysis for the prediction of ventricular arrhythmias in patients with ischemic cardiomyopathy," *Circulation: Arrhythmia and Electrophysiology*, vol. 13, no. 4, p. e007975, 2020.

[36] S. Zhou, A. AbdelWahab, J. L. Sapp, E. Sung, K. N. Aronis, J. W. Warren, P. J. MacInnis, R. Shah, B. M. Horáček, R. Berger, H. Tandri, N. A. Trayanova, and J. Chrispin, "Prospective multicenter assessment of a new intraprocedural automated system for localizing idiopathic ventricular arrhythmia origins," *JACC Clin Electrophysiol*, vol. 7, no. 3, pp. 395–407, 03 2021.

[37] N. A. Trayanova and E. J. Topol, "Deep learning a person's risk of sudden cardiac death," *The Lancet*, vol. 399, no. 10339, p. 1933, 2022.

[38] K. N. Aronis, A. Prakosa, T. Bergamaschi, R. D. Berger, P. M. Boyle, J. Chrispin, S. Ju, J. E. Marine, S. Sinha, H. Tandri *et al.*, "Characterization of the electrophysiologic remodeling of patients with ischemic cardiomyopathy by clinical measurements and computer simulations coupled with machine learning," *Frontiers in Physiology*, vol. 12, p. 684149, 2021.

[39] M. C. Waight, A. Prakosa, A. C. Li, N. Bunce, A. Marciniak, N. A. Trayanova, and M. M. Saba, "Personalized heart digital twins detect substrate abnormalities in scar-dependent ventricular tachycardia," *Circulation*, vol. 151, no. 8, pp. 521–533, 2025. [Online]. Available: https://www.ahajournals.org/doi/abs/10.1161/CIRCULATIONAHA.124.070526

[40] J. M. de Bakker, F. J. van Capelle, M. J. Janse, S. Tasseron, J. T. Vermeulen, N. de Jonge, and J. R. Lahpor, "Slow conduction in the infarcted human heart. 'zigzag' course of activation." *Circulation*, vol. 88, no. 3, pp. 915–926, 1993. [Online]. Available: https://www.ahajournals.org/doi/abs/10.1161/01.CIR.88.3.915